J MATER RES TECHNOL. 2019;8(6):6275–6288

Available online at www.sciencedirect.com

jmr&t
Journal of Materials Research and Technology
www.jmrt.com.br

Original Article

Microstructure and crystallographic orientation evolutions below the superficial white layer of a used pearlitic rail

Mohammad Masoumi[a,*], *Nelson Batista de Lima*[b], *Gustavo Tressia*[c], *Amilton Sinatora*[c], *Hélio Goldenstein*[d]

[a] *Universidade Federal do ABC, Centro de Engenharia, Modelagem e Ciências Sociais Aplicadas, Santo André, SP 09210-580 Brazil*
[b] *Instituto de Pesquisas Energéticas e Nucleares-IPEN, São Paulo, SP, 05508-900 Brazil*
[c] *Instituto Tecnológico Vale, Av. Juscelino Kubitschek 31, Bauxita, Ouro Preto, MG 35400-000, Brazil*
[d] *Escola Politécnica da Universidade de São Paulo, Departamento de Engenharia Metalúrgica e de Materiais, São Paulo, SP, 05508-030, Brazil*

ARTICLE INFO

Article history:
Received 24 June 2019
Accepted 9 October 2019
Available online 12 November 2019

Keywords:
Severe plastic deformation
White layer
Crystallographic texture
EBSD

ABSTRACT

Although several studies have been conducted on the mechanism of the formation of white layer by cyclic large shear deformation, and its effect on rolling contact fatigue, limited research has been carried out to find a correlation between sub-superficial layer of running contact surface and the crystallographic orientation, microstructural changes, and distribution of shear deformation and dislocation density. In order to understand the microstructural evolution (i.e., microstructure and crystallographic orientation) a used pearlitic rail sample removed from the heavy-haul railroad was investigated in the current work. A very thin superficial white layer was observed, approximately 15 μm below the running contact surface. X-ray diffraction analysis confirmed the formation of a supersaturated ferrite phase with carbon content of approximately 3.78 C wt%. It could be attributed to the cementite dissolution due to severe shear and compressive stresses, during intense shear plastic deformation, from the rail-wheel interaction. The dominance of {110} ferrite grains parallel to the rail direction was characterised, in the transition layer between white layer and non-deformed pearlite structure, by X-ray diffraction and electron backscattered diffraction techniques. Formation of these grains, corresponding to the closed-pack plane of the ferrite matrix at the transition region, leads to great ductility and retarded crack formation.

1. Introduction

Pearlitic rail steels are still widely used as the major railway type steels around the world, due to their high strength

---

* *Corresponding author.*
E-mail: mohammad.m@ufabc.edu.br (M. Masoumi).

https://doi.org/10.1016/j.jmrt.2019.10.021

and excellent wear and fatigue failure resistance. Pearlite structures exhibit good wear resistance under rolling-sliding conditions and abrasive modes [1–3]. Alternative layers of ferrite and cementite act as barriers to the moving dislocation, which leads to superior work-hardening [4]. Improvements of cleanliness, reduction of inter-lamellar spacing and thick cementite lamella can also improve the wear resistance [5]. In addition, higher plastic flow and fracture strain of fine pearlite causes higher wear resistance [6]. Finer pearlite colonies hinder the penetration, and subsequent material removal, by abrasives, resulting in shallow abrasion. On the other hand, the formation of the continuous network of cementite at the prior austenite grain boundaries, increases the brittle fracture and cracking along the boundaries [7].

Pearlitic steels, with high carbon-manganese content and without any major alloying elements, are subjected to intense plastic deformation caused by high axle loading from passing trains. This result in serious wear and a transformed surface structure, which is called the white etching layer (WEL). The white etching layer is more brittle than the pearlitic base material and can enhance crack initiation and propagation, leading to early fracture in rails [8,9]. There are two main hypotheses, assumed, for the formation of white layer. One is martensite formation due to the temperature rising to austenitisation temperatures because of the flash heating, in the order of milliseconds, due to the wheel-rail friction contact by adiabatic shear instability, then the subsequent martensitic transformation due to rapid quenching [10–12]. The second hypothesis is the formation of, highly distorted, carbon supersaturated nanocrystalline ferrite due to the decomposition of cementite in pearlitic steel during severe plastic deformation, followed by dragging of the carbon atoms from the cementite into the ferrite lattice [13–15].

Olofsson et al. [16] studied the development of wear and plastic deformation damage mechanisms on two rails for 2 years. They reported a significant change in the rail profile due to wear and unidirectional plastic strain accumulation (ratcheting) during the service period. In addition, the wear rate increases by increasing the severity of the contact pressure and sliding velocity, leading to a change of wear mechanism from mild wear to severe wear. Mild wear dominated at the railhead, exhibits a smooth surface rather than the original surface. However, severe wear form at rail edge, associated with seizure results in a rougher surface rather than the original surface [17]. In other words, squats defect generally formed at railhead initiates by exhausting the surface material (ratcheting) or fatigue mechanism (shakedown) due to the cyclic high contact stress. Moreover, the microhardness values at the WEL adjacent to squats are 2–3 times higher than the original state, confirming the brittle nature of WELs and enhancing fatigue crack initiation as well.

The dislocation movements on the active slip systems are responsible for plastic deformation under external loading. Owing to the pioneering work of Schmid law [18], a slip system is activated when its resolved shear stress reaches a critical value (CRSS). However, Taylor pointed out that BCC materials do not obey Schmid's law, due to the lack of mirror symmetry with respect to planes orthogonal to the dominant <111> slip direction [19]. Owing to the multiplicity of slip systems in BCC materials, there are 48 slip planes: 12 {110}, 12 {112}, and 24 {123} planes. However, plastic deformation is governed only by the motion of <111> screw dislocations associated with the densest direction [18,19]. In this regard, (100) crystallographic planes are known as the main cleavage planes. While, the {110}<111> and {112}<111> are the main slip systems and depends on temperature and strain rate. On the one hand, according to the von Mises, at least five independent slip systems are required for plastic deformation. On the other hand, the grain deformation has to accommodate its neighboring grains [20]. Therefore, plastic deformation happens when two neighboring grains might rotate in a pattern to make their orientation closer. To this end, orientations corresponding to the compact planes at boundary would enhance deformation by increasing the geometrical accommodation of adjacent grains [21].

It is well-known that white layer plays a critical role in crack initiation and propagation, on the rail surface, which reduces wear resistance and lifetime. Recently, the characterisation of microstructural evolution, in depth from the distance, and its effects on macro-scale mechanical properties (i.e., tensile strength, fracture toughness and crack propagation), was proposed to optimise wear behaviour [22–25]. Satoh et al. [22] analysed the effect of crystal orientation on a used pearlitic rail using X-ray diffraction and electron backscatter diffraction (EBSD). They reported the development of {111} crystallographic orientation of grains, oriented parallel to the running surface, up to about 100 μm in depth from the surface. Solano-Alvarez et al. [26] observed that subsurface fatigue cracking initiated at inclusions and propagated through brittle {001} grain boundaries. Matsuda et al. [24] also documented the relationship between the rail damage, and crystallographic changes, due to the accumulation of micro-strain, or fatigue, on the running surface. Guo et al. [25] documented the development of {110} fibre texture of ferrite matrix due to the formation of deformation bands, and shear-like bands, by heterogeneous deformation of pearlite colonies and ferrite-cementite interfaces, during wire drawing, in pearlitic steel. This evidence points to similar plastic shear deformation of the cementite lamellae and cementite/ferrite phase boundaries, during the life of rails in heavy haul railways.

Hence, most of the research has focussed on the influence of microstructure modification, rather than the influence of texture, on tribological behavior [22,24,26]. The fatigue behaviour is affected by the structural evolutions, such as changes of the crystal orientation, coefficient of friction, subgrain size, and local strain distribution of the deformed surface and subsurface layer [27]. The crystallographic orientation, changes of preferred direction, and its discrepancy also control the tribological properties, due to the activated glide systems in the tribological contact for dislocation movements. EBSD and X-ray diffraction (XRD) were employed to characterise the microstructural evolution (i.e. microstructure and crystal orientation) on WEL and the sub-superficial layer of the running contact surface. Therefore, detailed characterization of the microstructural gradient evolution along the rail depth including subjected to severe rolling-sliding modes were investigated in a used pearlitic rail sample, to understanding the microstructure modification including partially dissolved parent cementite in the WEL and formation of nanocrystalline carbon-supersaturated ferrite accompanied by crystallographic grains rearrangement at micrometer scale.

2. Material and procedures

The specimens were removed from an inner curved rail track with a radius of 344 m, containing slightly surface defects which shown in Fig. 1. The rail track has a total load passage of approximately 38 million gross tonnages (MGT) for a period of 4 years in-service. A series of head check defects were generated on the fatigued rail sample due to severely cyclic a plastic deformation between the wheel and the rail. In this research, the maximum value of the crack depth from the surface of the railhead is about 10 μm and does not pass the WEL. The chemical composition of two investigated rail steel (in the original and fatigued states) identified by spectrometric analysis about 10 mm from the rail surface, was (in wt.%) 0.75C, 0.22Si, 1.03 Mn, 0.019 P, 0.005S, 0.21Cr, and 0.05Ni.

The microstructure was analysed using scanning electron microscope (SEM, FEI-Inspect F50) as a function of different distances from the contact surface, sectioned along the transverse direction. Metallographic preparation of the samples involved hot mounting, in non-conductive bakelite (at 160 °C for 5 min), followed by manual grinding using silicon carbide papers from 100# to 1200#, polishing with 6, 3 and 1 μm water-based diamond suspensions, and etching by 4% Nital (4 vol% nitric acid and 96 vol% alcohol) solution for 30 s.

The hardness variation, as a function of distance from the railhead, was also measured for the transverse section of railhead by microhardness and nano-indentation techniques. Microhardness was carried out using a Shimadzu (HMV-2TADW) tester with 4.903 N load ($HV_{0.5}$) and 15 s dwell time. Nano-indentation testing was conducted using the Triboindenter TI 950 (Hysitron Inc.), involving an array of 10 × 5 indentations in 50 × 50 μm, applying a load of 10 mN and using a Berkovich type indenter. Reduced Young's modulus (Er) and nano-hardness (H) values, of each indentation point, were calculated using Dao et al. [28] methodology for the implementation of the reverse algorithm on load-depth curves obtained by nano-indentation.

Two samples, with a length of 250 mm, width of 200 mm, and a thickness of 2 mm, were cut off in a longitudinal direction from the rail surface, before and after service (known as original state and fatigued rails samples), for X-ray diffraction (XRD). X-ray phase identification was performed using an X-ray diffractometer (Philips, X'Pert MPD) in Ψ-geometry employing Cu- K_α radiation. Phase analyses were performed in a 2θ-range between 30° and 120° with 0.001 2Theta step size. The X-ray peak broadening corresponds to the state of the exhausted microstructure during service and the residual microstrain within the crystallites. These two parameters can be deconvoluted by plotting the peak width at half the maximum height (in radians) $K = 2sin\theta/\lambda$ where θ is the Bragg angle and λ is the X-ray wavelength. Furthermore, standard strain-free crystals of LaB6 were diffracted in the same instrument, over a 2Θ range of 20-150°, in order to measure the instrumental broadening using the Caglioti equation [29]:

$$\beta_{standard} = \sqrt{utan^2\theta + vtan\theta + w} \quad (1)$$

where β is the physical widening for a specific *hkl* plane; and $u, v,$ and w were obtained as 0.00467, 0.003902, and 0.001037 after full diffraction profiles (i.e., (110), (200), (211), (220), and (310)) fitting by the Rieveltd method using the GSAS (General Structure Analysis System) software. Furthermore, modified Williamson-Hall plots were made for the ferrite peaks for an estimation of the dislocation density. In order to obtain better analysis a pure Lorentzian, or a Gaussian shape, was implemented according to ref. [30].

The carbon content in the ferrite gradually increased under rolling/sliding conditions. The percentage of dissolved carbon (X_c), in ferrite super saturated α-iron, has been calculated from the lattice parameter for the exhausted ferrite [31],

$$a_\alpha = a_0 + \frac{(a_0 - 0.279x_C)^2 (a_0 + 2.496x_C) - a_0^3}{3a_0^2} - 0.03x_{Si} + 0.06x_{Mn} + 0.07x_{Ni} + 0.31x_{Mo} + 0.05x_{Cr} + 0.096x_V \quad (2)$$

The same XRD samples were used to obtain crystallographic texture analyses. The macrotexture was measured by an X-ray diffractometer (Philips, X'Pert MPD). The diffracting positions of each sample were accurately selected, initially, by high-resolution X-ray measurements. Then, incomplete pole figures (i.e., {110}, {200}, and {211} reflections of ferrite matrix in pearlite structure) were obtained from the three reflections, measuring azimuth angles between 0–350° and polar angles between 0° and 80° at a 5° step size. Then, the orientation distribution function (ODF) was calculated using M-tex [32] free Matlab toolbox for analysing and modelling crystallographic textures.

Electron backscattered diffraction (EBSD) analysis was performed using a TSL EDAX system installed on a FEI-SEM with the working distance of about 12 mm, ×5000 magnification, 5 spot size, and 50 nm step size. EBSD analyses were conducted for the same non-etched SEM samples. Final polishing, with 50 nm colloidal silica slurry for 3 h, was used in order to obtain the best Kikuchi pattern. Only the BCC ferrite phase can be indexed by EBSD, since fine cementite lamellae are below resolution of the EBSD system and so not able to produce indexable patterns. Finally, the detailed ESBD analysis was conducted by using TSL OIM analysis 7 and M-TEX software.

A cross-sectional foil for TEM was prepared by focused ion beam (FIB) technique using a FEI Quanta 3D FEG/FIB. Detailed microstructural features were characterized by Transmission Electron Microscope (TEM), equipped with Electron Energy Loss Spectroscopy (EELS) to map the chemical composition. TEM was operated at 200 kV, working with selected-area electron diffraction (SAED), nanobeam diffraction (NBD), conventional bright-field (BF), dark-field (DF), and high-resolution TEM (HRTEM) imaging.

3. Results and discussion

The fine pearlitic microstructure of the original virgin (as-received) rail steel was investigated using SEM and is presented in Fig. 2. A non-uniform cementite lamella thickness along rail lines is inevitable during production process. Pearlitic microstructure with interlamellar spacing

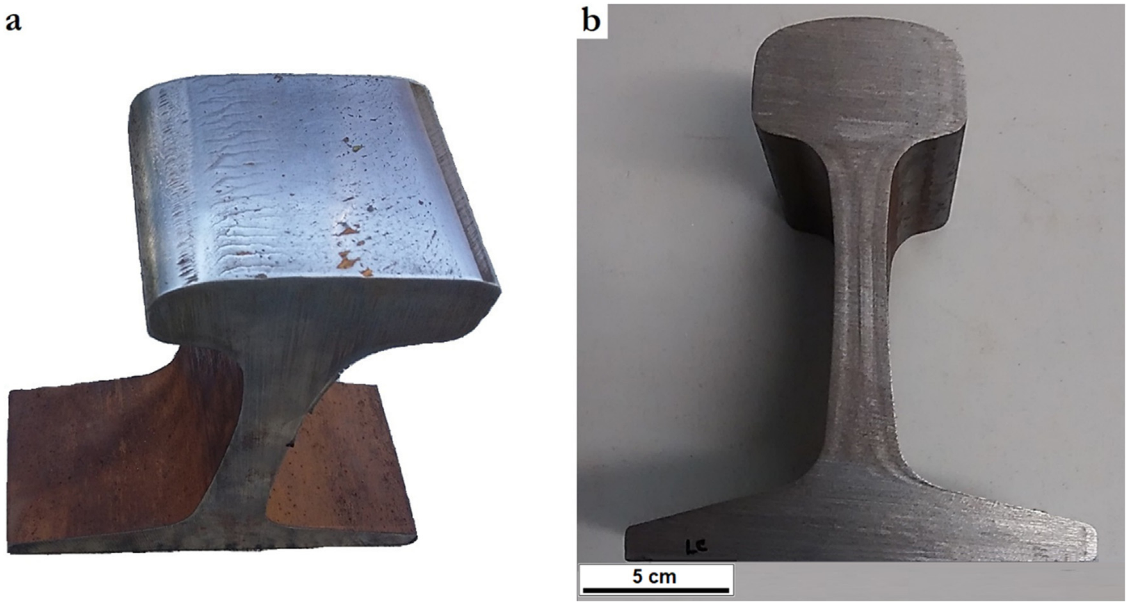

Fig. 1 – (a) Worn pearlitic rail steel removed from heavy-haul Brazilian railroad and (b) transversal section.

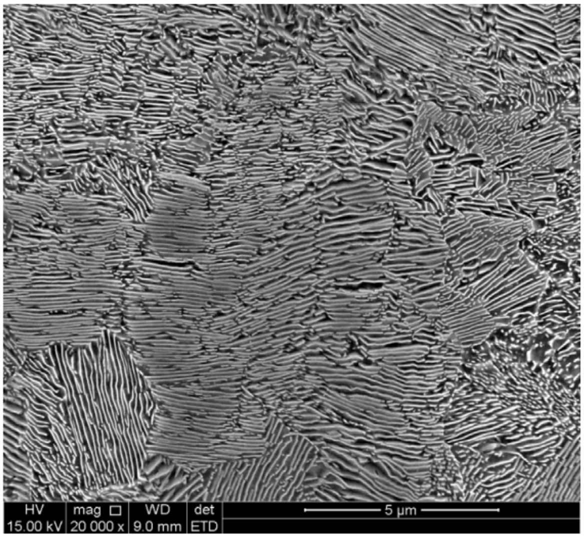

Fig. 2 – SEM micrographs of as-received, original virgin rail steel (ferrite in dark and cementite in bright contrast).

and pearlite colony sizes of approximately ≈90 ± 30 nm and 15 ± 5 µm were characterized in the original state of rail sample. It is well documented that refined pearlite, with fine interlamellar spacing (less than 200 nm), improves the hardness and work hardening behaviour by means of restricted dislocation movement. Consequently, the fine interlamellar spacing can prolong the service life of pearlite rails by increasing the wear resistance. Notably, the interlamellar spacing gradually increases along the railhead due to the cooling rate. Superficial hardening treatments involve heating the railhead followed by fast continuous cooling are conducted pearlitic steels for railroad application to enhance wear properties [33]. In this treatment the railhead is heated to 900 °C followed by accelerated cooling at a high critical cooling rate (10 °C/second) for reduction of the austenite to pearlite transformation as low as possible (about 550 °C) to form a refined interlamellar spacing. In contrast, the difference in the expansion coefficients of ferrite and cementite, under pearlite transformation, forms residual stress and elastic strain [34], which could have a negative effect on early crack initiation due to lattice non-compliance at the interfaces of the ferrite and adjacent cementite. On the one hand, the large pearlite interlamellar spacing avoids the overlap region between the lattice distortions at the ferrite/cementite interfaces. On the other hand, very small pearlite interlamellar spacing leads to an overlapping of the two strain areas, such that the ferrite hardening reaches saturation, leading to the formation of microcracks at the interface of ferrite and cementite. Therefore, the refinement of interlamellar spacing, accompanied by simultaneously refining ferrite and cementite, can increase the plasticity [35].

Fig. 3 shows the evolution of pearlite microstructure as a function of depth from the rail surface. Non-deformed pearlite colonies, with no preferred colony orientations, were observed approximately 50 µm below the surface area, as seen in Fig. 3b. The average pearlite colony diameter and the average pearlite interlamellar spacing were estimated to be about ≈ 18 µm and ≈ 100 nm, respectively, measured using the circular line method [36]. Although non-uniform cementite lamella thickness and interlamellar spacing can have effect on strain distribution, its slight difference along rail line could be neglected. The hardness, in this non-deformed pearlite area, was about 375 ± 15 HV. Ferrite-cementite interfaces act as barriers to dislocation movement causing increased hardness and yield strength, according to the Hall-Petch theory [37], which can improve wear resistance. During train circulation, the cyclic compression-tension shear stress on the rails leads to an accumulation of plastic deformation and an increase in the shear stresses, causing the gradual structure variation

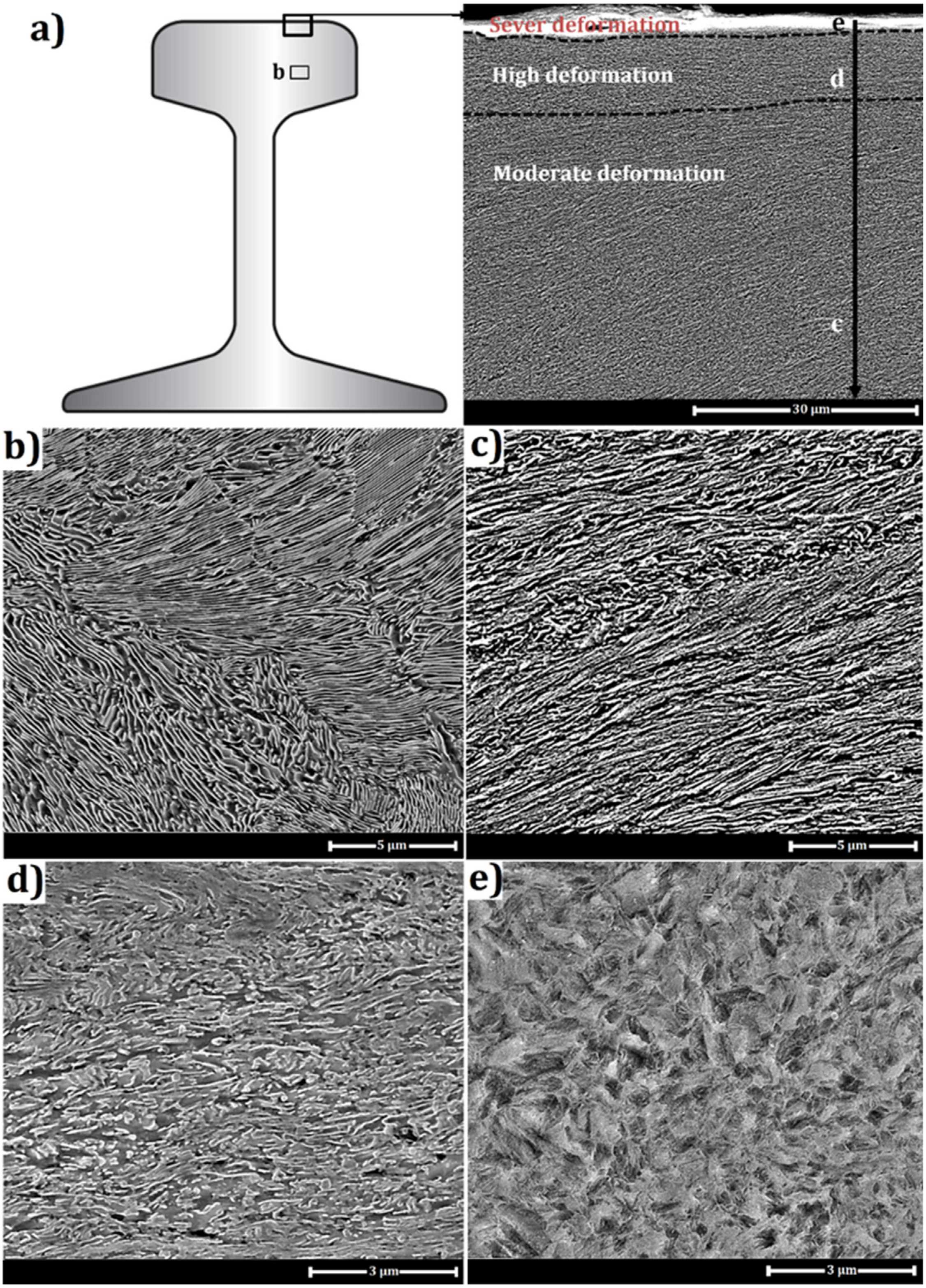

Fig. 3 – (a,b) Transversal section of headrail surface and (c–f) microstructural alterations as a function of surface depth.

along depth distance [38]. Thus, the deformation level rises continuously towards the rail surface.

Fig. 3c shows the aligned pearlitic microstructure (cementite and ferrite structure parallel to shear bands), approximately 15–50 μm below the rail surface, due to high tangential shear stresses in the rail contact surface [39]. The hardness value, in this area, increased up to around 425 HV. Then, a highly deformed pearlitic structure, containing thinning, bending, and fragmenting of cementite particles was observed a few microns ($\approx$15 μm) below the rail surface, Fig. 3d. Toribio et al. [40] and Guo et al. [41] explained the changes of pearlite morphology by rotational movements when the two ends of pearlite lamellae received the same compressive stress, perpendicular to the rolling direction. Kink, or shear band, also enhances the fragmenting and re-orientation of cementite layers [40,41]. Microhardness measurements showed a continuous increase of hardness to about 465 HV in this deformed region. Embury and Fisher [42] reported that the bent and broken cementite structure acts as a barrier to dislocation motion, leading to significant increases in strengthening and more dislocation pile-ups, due to more ferrite-cementite interfaces. Finally, a featureless (featureless in the sense that the characteristic lamellar pearlitic morphology is no longer visible, Fig. 3e) WEL structure, with extreme microhardness values about 835 ± 15 HV, was characterised close (≈10 μm) to the rail surface. In general, work hardening in pearlite can barely increase any higher than 500 HV. Such an extremely high hardness could be explained by the formation of martensite induced cyclic plastic deformation. A combination of severely plastic deformation depends on cyclic wheels loading, high pressure, and local temperature increase results in formation martensite induced cyclic plastic deformation [26,43].

The nano-hardness testing was conducted at 5 μm below the contact surface. The principal objective of the nano-indentation test is to obtain elastic modulus and nano-hardness values of the rail sample, along the surface depth from experimental nano-indentation load-displacement measurements, using readings of the indenter. Unlike a conventional microhardness method, the size of the projected contact area, and related residual impression, are too small. Thereby, accurate mechanical properties, and elastic-plastic behaviour, can be obtained from load-depth curves. In nano-indentation testing, force and depth of penetration are recorded when a load is applied from zero to a maximum, holding steady at the maximum load, and then from maximum force back to zero [44]. Nano-indentation hardness values were about 5.5 GPa (about 509.8 HV) only 50 μm below the surface, while its value increased strongly to reach approximately 7.9 GPa (718.9 HV) very close the contact surface ≈15 μm. Experimental load-displacement curves, obtained by a Berkovich type indenter and 10 mN force, are shown in Fig. 4a. Reduced Young's modulus and nano-hardness values were calculated using the reverse algorithm proposed by Dao et al. [28], and are presented in Fig. 4b. A continuous reduction in both nano-hardness, and reduced Young's modulus, was observed as a function of distance from the rail surface. Reduced Young's modulus dropped from 200 ± 3 GPa to 186 ± 3 GPa at only 50 μm from the used rail surface.

Hence, the nanoindentation measurements exhibited a large scatter due to the inhomogeneity of the microstructure, the modulus of elasticity was continuously decreased from WEL region to undeformed pearlite. In general, the tendency of Young's Modulus would depend on grain size below micro-meter level. This is attributed with the increase in the volume fraction of grain boundaries, leading to weaken atomic bonding at grain boundaries and triple junctions, consequently deleterious eff ;ect for the elastic modulus [45]. On the other hand, the crystal orientation of each grain governs the crystal local Young's modulus of o each grain based on a geometrical assumption. Masumoto et al. [46] showed that the largest Young's modulus calculated from the resonance frequency of vibration (500–800 Hz) in carbon steel is near to the <111> and <110> direction and the smallest in <100> direction (i.e., $E_{<111>} > E_{<110>} \gg E_{<100>}$). The results suggest that excessive cyclic loads, due to passing trains, significantly increase the elastic modulus. The significant increase of the reduced Young's modulus could be attributed to extensive residual stresses and large dislocation densities at superficial WEL and highly deformed sub-superficial layers [47]. The combination of high hardness and work-hardening capacity at the rail surface, and gradual decreases along the depth distance, are related to compressive residual stress due to cyclic rolling/sliding loading, which can increase fatigue life [3]. The accumulated residual tensile or compressive stress enhances fatigue crack initiation due to exhausted ductility of a material. However, the higher compressive residual stress ahead of crack tips delays fatigue crack propagation, which increases fatigue life [48]. It is also expected that the excess hardness value, at the rail surface, prevents material removal by abrasives, resulting in high wear resistance.

It has been reported [14,15] that the high dislocation density generated by severe plastic-deformation, absorbed at the cementite/ferrite interfaces, lead to cementite decomposition in the non-equilibrium condition. Thereby, carbon-supersaturated ferrite, with very high crystal distortion, forms at superficial, severely deformed, contact regions. X-ray diffraction analysis was conducted on the rail surface, before and after service, to understand structural changes due to tangential shear and normal stress as well as contact temperature. Fig. 5 shows the X-ray diffraction patterns which characterised both ferrite and cementite, with the more intense peaks corresponding to the matrix ferrite phase. X-ray diffraction data demonstrated an approximate 20% peak broadening in comparison with the initial state due to the residual microstrain within the crystallites under the rolling/sliding condition. The as-received, non-deformed, pearlite microstructure had approximately 7% cementite, with this amount reducing to about 2% in the used rail sample. This effect could be explained by interlamellar spacing, with the cementite lamellae becoming thinner in the pearlite structure. However, the appearance of a kink (left side) in the {110} α' peak was validated by the Lojkowski et al. [12] results. They reported that dense dislocation walls or clouds, at the pearlite/cementite interface, might be contributing to the fragmentation of cementite and the dissolution of carbides. Carbon atoms settled at dislocation cores with low energy sites, leading to the formation of a super-saturated α iron phase with a higher lattice parameter and nanocrystalline sizes at the surface layer [13–15]. From this observation and the hardness results (i.e., microhardness and nano-indentation), it is confirmed that the featureless WEL structure region is a nanocrystalline ferrite structure in which cementite particles are dissolved.

The XRD pattern can estimate the ferrite lattice parameter, the carbon concentration of ferrite and the dislocation densities in the ferrite matrix of the pearlite structure. The lattice parameter of the as-hot rolled, non-deformed structure was about 2.866 Å, while the lattice parameter of the severely deformed ferrite matrix, at the running surface, was calculated to be 2.877 Å. Also, the dislocation density was

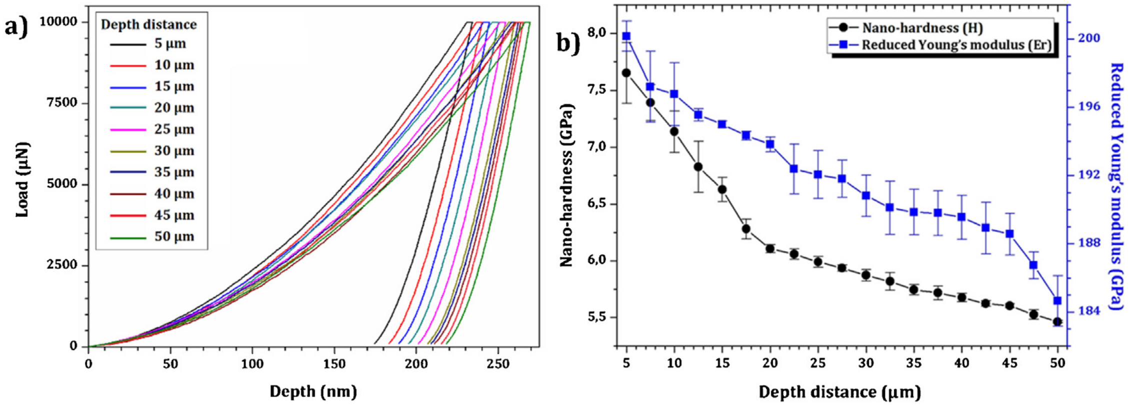

Fig. 4 – (a) Experimental load-displacement curves and (b) variation of nanohardness and reduced Young's modulus along depth distance from the rail surface.

estimated as approximately 6.77×10^{14} and 1.43×10^{16} m^{-2}, before and after rolling/sliding condition, respectively, by means of the physical broadening of each specific *hkl* peak. This estimate depends on the crystallographic defects and the nanocrystalline structure formed in the carbon supersaturated iron phase. It is worth mentioning that the higher dislocation density at the contact surface, due to the formation of nanocrystalline carbon supersaturated ferrite by severe plastic deformation, is consistent with excessive hardness increments close to the contact surface. Although Wu [11] presented that the austenization temperature is decreased by hydrostatic pressure, no meaningful retained austenite was found using XRD investigation at used rail sample. It might be implied that all low stability (probable) retained austenite at the near surface transformed into martensite during the servicing.

The carbon concentration of the ferrite phase can be estimated from the lattice parameter, in order to understand and confirm carbon migration by severe deformation, but accurate measurement of the carbon concentration from the ferrite lattice is problematic due to difficulties such as crystallite size effects, heterogeneous distribution of carbon in ferrite and the breaking of crystal symmetry [49]. The percentage of dissolved carbon atoms, in two distinct micro and nano (super-saturated) ferrite phases, was estimated as 0.02 and 3.78% using Eq. 2. It is suggested that the cementite decomposition, which occurred under severe shear strain close to the wear surface, was induced by carbon dissolution into a dense

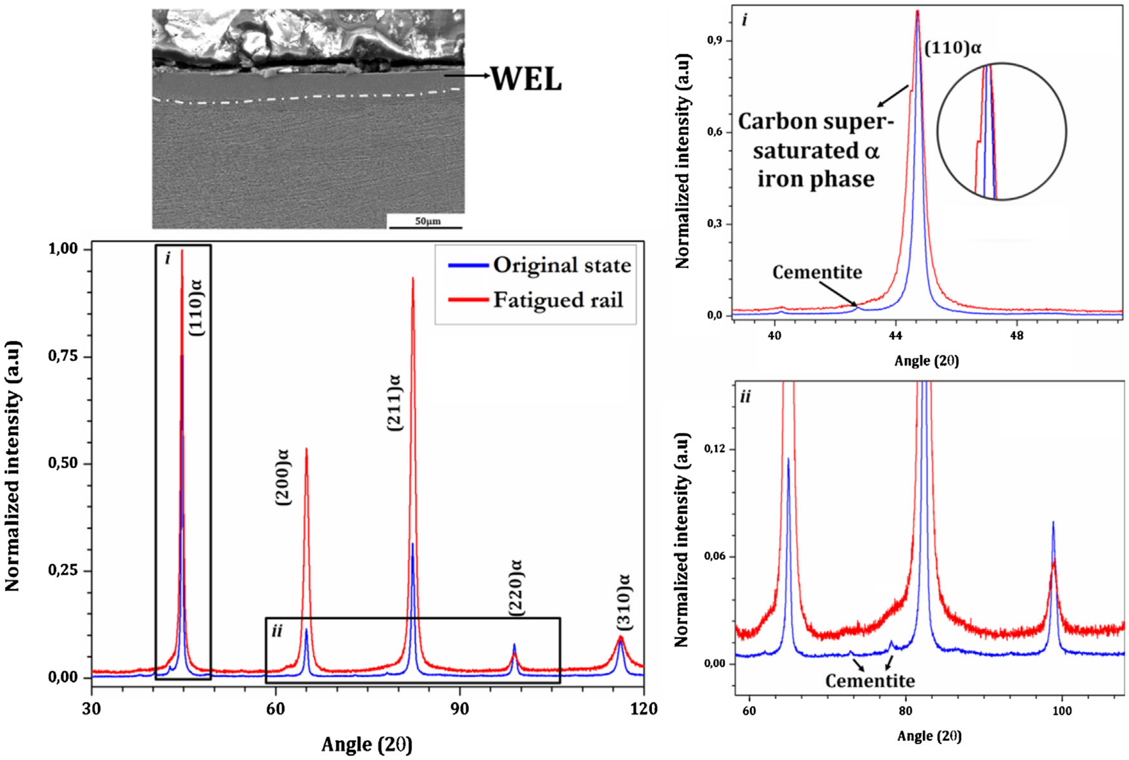

Fig. 5 – X-ray diffraction pattern profiles obtained from the plane parallel the railhead surface before and after rail service.

dislocation wall ferrite interphase, leading to the formation of nanocrystalline super saturated ferrite. The higher concentration of carbon in the ferrite phase leads to an increase in the lattice parameter and on the emergence of a new peak, at a lower incident angle, that can be seen in Fig. 5. The carbon enriched ferrite lattice is detected as a separate ferrite phase, also with body-centered cubic crystal structure, but with an expanded lattice parameter. Cyclic compression-tension shear strain, at the rail surface, resulted in rapid multiplication of dislocations at the ferrite/cementite interphase. Experimental results [14,15,50] demonstrate the gradual cementite structure decomposition during severe plastic deformation, in which the carbon atoms segregate to microstructural defects, such as dislocation walls or grain boundaries, of the ferritic matrix. Sauvage et al. [14] also studied the distribution of carbon atoms by the dissolution of cementite, and found that the dissolution of 20–50% of the cementite increases the carbon content in ferrite up to 4.4%. Li et al. [51] estimated that the binding energy, between dislocations in ferrite and carbon atoms, is higher than the interaction between carbon atoms in cementite. Thus the increased dislocation density, elastic stresses and large quantity of new boundaries where carbon atoms can segregate, can explain the cementite dissolution. Therefore, a nanocrystalline, C supersaturated iron phase was formed in the contact surface layer.

Transmission electron microscopy (TEM) is capable of resolving details down to crystal atomic planes, because the electron beam is generated by applying a high electrical field. In addition, the electron-transparent specimen accompanied by a high energy electron beam reduces the beam/specimen interaction volume, rather than SEM images, thus obtains an excellent spatial resolution. Fig. 6 presents the high-resolution bright-field TEM micrographs and corresponding nanobeam diffraction (NBD) pattern obtained at the transition zone between the pearlite (green area) and WEL (blue zone) regions. An apparent microstructure change was distinguished in these regions by the bright field micrograph and confirmed by NBD patterns. In the green area, some cementite (Fe_3C) lamellae were found within the ferrite matrix, indicating the pearlite microstructure. The presence of cementite in this region (about 3 μm beneath the railhead surface) was confirmed by the corresponding selected area electron pattern and the cementite indexing. The bright-field micrograph at the WEL exhibited the tetragonal crystal structure (bct) with no cementite particles. Thus, it is concluded that the pearlite is completely changed to the martensite at the WEL region. It is worth mentioning that no retained austenite was found at the regions analyzed at WEL, as well. To provide a clear observation, chemical mapping of Fe and C elements was analyzed along depth distance (black zone). The inhomogeneous distribution of carbon along depth distance clearly shows the dissolution of cementite to form the supersaturated carbon tetragonal crystal structure.

Macrotexture analysis, by X-Ray Diffraction, provides quantitative information about the distribution of crystallographic and grain orientations developed during the

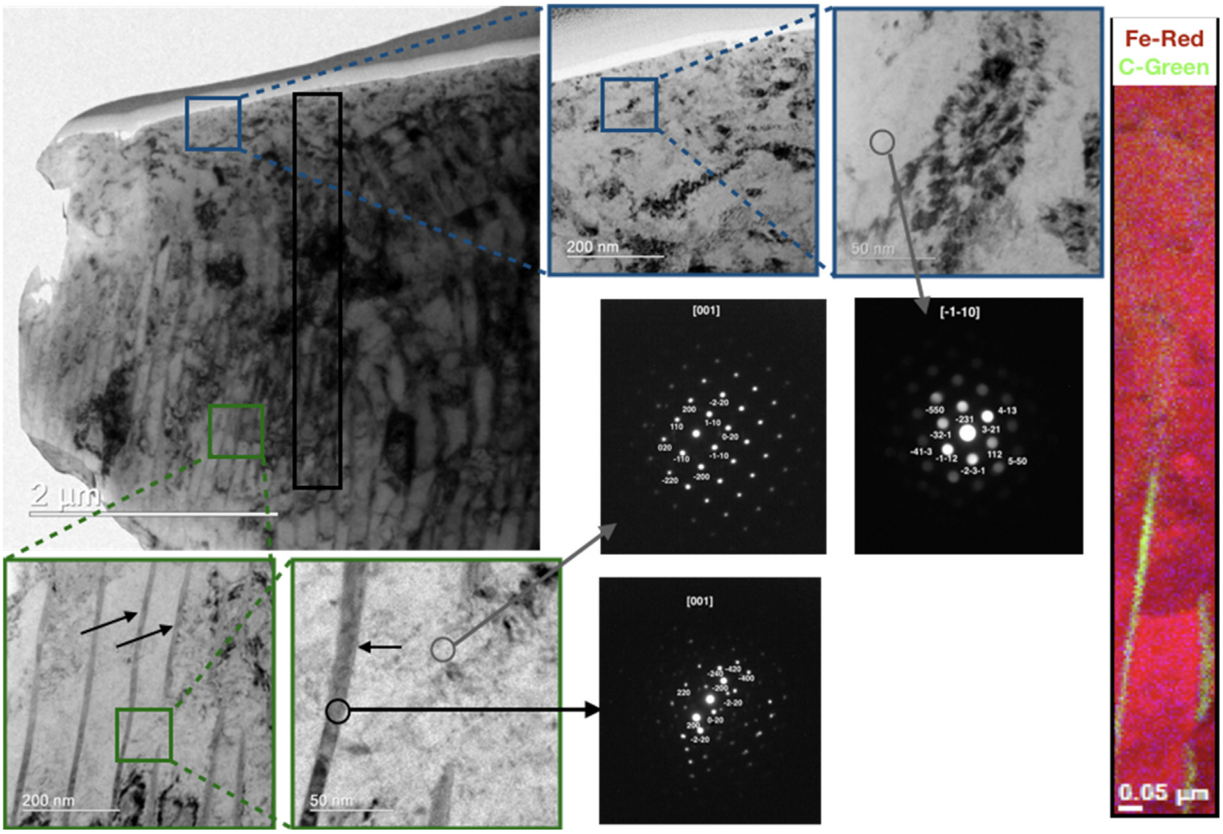

Fig. 6 – High-resolution bright-field TEM micrographs and corresponding nanobeam diffraction pattern obtained at the transition zone between the pearlite and WEL regions accompanied with chemical mapping of Fe and C elements analyzed along depth distance.

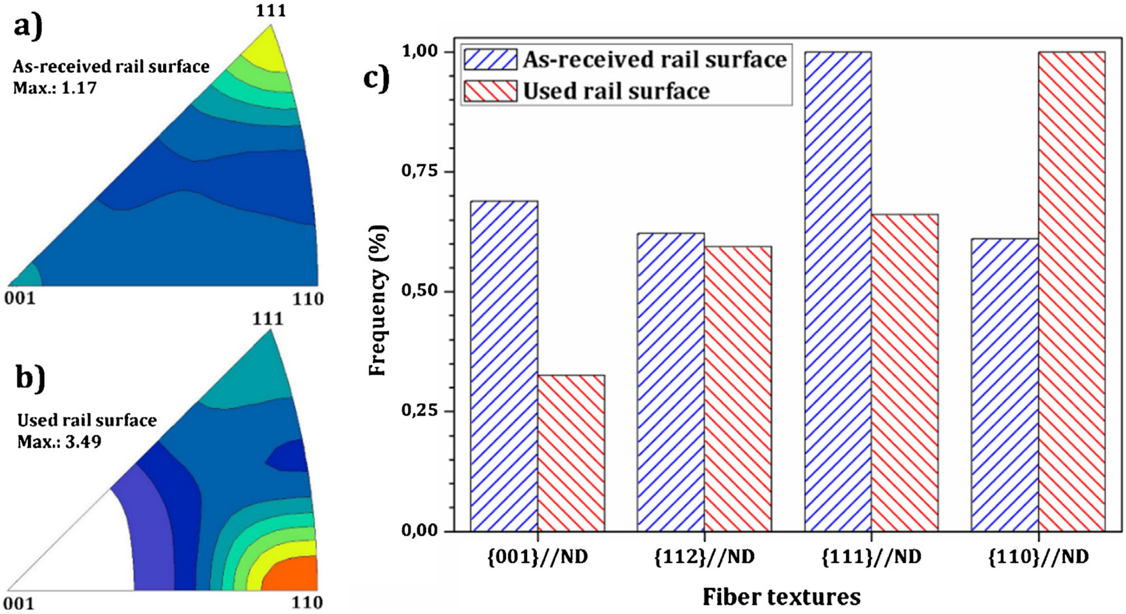

Fig. 7 – Normal direction IPFs at (a) as-received, (b) used rail contact surface samples, and (c) quantitate comparison of normalized fiber intensities in common BCC structure of pearlite matrix.

manufacturing process and service period. This can demonstrate the effect of vehicle steering forces on changes of grain orientation, which can be used to predict mechanical properties at the surface layer of rails. The normalised quantitative comparison of the common fibre textures (i.e., {001}, {112}, {111} and {110}//ND) and their inverse pole figures (IPF), at rail surface of both the as-received and used rail samples, are shown in Fig. 7. A random crystallographic texture with a slight fraction of grains aligned to {111}, plans parallel to the normal surface direction (ND), was identified in the as-received rail surface, Fig. 7a. The slight {111}//ND texture is typical due to the hot rolling during the rail manufacturing process. However, a predominantly {110}//ND fibre texture was characterised at the contact surface of the used rail, Fig. 7c. The inhomogeneity of the crystallographic texture along the surface depth of the used rail is related to the deformation caused by the friction between the wheels and the rail, during the passing of trains, and corresponds to shear texture close to the contact surface. Guo et al. [52] reported that the <110> fiber texture formed during wire drawing of fully pearlitic steel, exhibits a soft orientation for dislocation slip, while all the neighboring colonies are in hard orientations around <110> direction. Such a different behaviour arises from a large number of deformation bands and shear-like bands, leads to generate a localized inhomogeneous deformation. The development of {110} grains is associated with the plane strain deformation. Guo et al. [52] showed the decrease in stress concentration is due to rotation of ferrite and cementite lamellae into <110> direction during the cold drawing of pearlite. The comparison of quantities of the fibre intensities also showed the rotation of {001} and {111}//ND texture into {110}//ND due to plane strain deformation caused by the train passing at the rail surface.

The colour-codded IPF represents the orientation of the sample reference axis in the crystal reference system. The orientation distribution function (ODF) can characterise the crystallographic directions by the Euler angles $(\varphi_1, \phi, \varphi_2)$ and Miller indices (hkl)[uvw] (which (hkl) cube planes are parallel to the rail normal plan and [uvw] directions are parallel to the rail direction). ODFs were estimated from EBSD maps by means of the statistical kernel density estimation method by M-TEX software [32] and plotted at constant $\varphi_2 = 45^\circ$ of Euler angles. Fig. 8a shows that the normal direction of the rail in unused rail is oriented with an intensity of 1.17 times more that the random along the <111> crystal direction and in the deformed (used) rail the rail normal direction is oriented along <011> crystal direction. Detailed crystallographic analysis revealed the formation of $(110)[1\ \bar{1}\ 3]$ to Goss (110)[001] crystal orientation, by rotation of {001} and {111}//ND textures, due to shear deformation. According to Suwas et al. [53], shear texture is represented by a shear plane {hkl} and the shear direction [uvw]. Thus, the most close-packed (110) plane of ferrite matrix formed, and developed, by increasing the plane shear strain. In addition, Guo et al. [25] reported that development of {110} texture is related to the fibre structure of pearlite morphology and the cementite alignment toward the drawing direction, which can enhance strength and toughness of cold drawn pearlitic steel wires. According to Sainath et al. [54] and Blondé et al. [55], grains oriented along {110} crystallographic planes show superior mechanical properties due to the nature of the interatomic forces and small interplanar distance in BCC structure. Thus, the presence of the {110} texture, at the running contact surface, can actually increase the local mechanical properties. Moreover, the highest values of reduced Young's modulus, obtained from nano-indentation results, can be related to the formation of {110}//ND crystallographic texture. Another critical issue is that the WEL region, with a polycrystalline structure, has a random crystal orientation. Thus, the {110}//ND grains are related to the transition

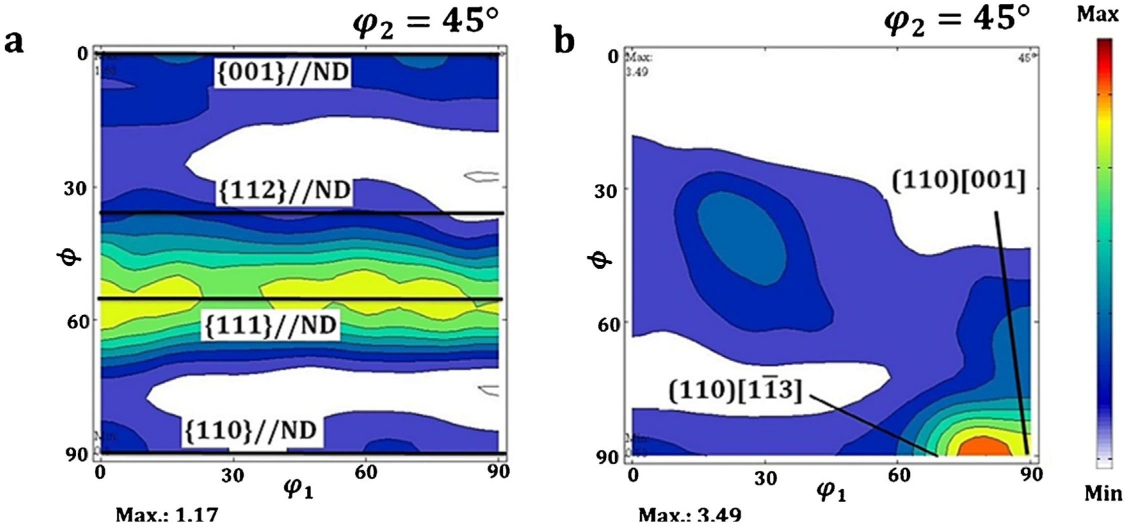

Fig. 8 – ODFs at constant $\varphi_2 = 45°$ of (a) as-received and (b) used rail contact surface samples.

zone in which cementite particles are aligned with the train moving direction.

Dislocation density is associated with the accommodation of a lattice curvature from a deformation gradient has been calculated by Geometrically Necessary Dislocations method using Nye-Kroner equations from EBSD data [56]. Bracquart et al. [57] investigated the influence of crystallographic orientation on the initiation of a fatigue crack by the EBSD technique. They pointed out that fatigue crack initiation is strongly dependent on the crystallographic orientation of the surrounding grain. This means, grains oriented to slip plans are more prone to crack initiation. Wan et al. [58] investigated the influence of crystallographic orientation on the Mises stress distributions to explain plastic shakedown or ratcheting. Accumulated slip in cyclic loading generates persistent slip bands causes increasing the local strain energy. Stored energy is considering the geometrically necessary dislocation (GND) densities and dislocation pile up due to lack of adequate slip systems, leads to the nucleation of a crack as well. Also, it is known that the stored energy generated by neighboring grains atomic misfit can concentrate localized strain, which enhances the crack initiation and crystal failure [59]. The variation of crystal orientation, fraction of high angle boundaries (HABs, random grain boundaries considered to point-to-point misorientation greater than 15°) and dislocation density as a function of depth from the running surface, has been calculated from the EBSD data and presented in Fig. 9. The significant increase of HABs found is evidence for the ultra-fine grain refinement due to severe deformation. Grain sizes of nano-crystalline BCC structure, at very superficial layer (≈10 μm distance depth), were approximately 500 ± 100 nm (step size of EBSD measurement was 50 nm). It can also be seen that both the fraction of HABs and the dislocation density had a maximum, close to the contact rail surface. The possible mechanism for this grain refinement, with the intense plastic deformation, is related to the excessive number of dislocation densities. Initially, a huge number of dislocations entangle at ferrite/cementite interfaces, ferrite grain boundaries, and sub-grain ferrite boundaries. Secondly, a high fraction of low angle boundaries (LABs, point-to-point misorientation of less than 15°) are formed by dislocation rearrangement in order to decrease the stored elastic energy. LABs are then transformed into HABs due to excess crystallographic defects with the high stored energy of dislocations at LABs. In other words, the immense dislocation accumulation and rearrangement, during severe plastic deformation close to the surface, leads to grain refinement. A gradual decrease in the HABs fraction and dislocation density, with increasing depth from the surface, was also observed.

The (001) direct pole figure, as determined in three small regions (5 × 5 μm) along depth distances, is also shown in Fig. 9. Regions *i* and *ii* presented specific grains in these small areas, at 20 and 40 μm from the rail contact surface. Pole figure calculated from superficial WEL (region *iii*) showed a nanocrystalline structure, with a wide range of random plane direction distribution, in a very small area. It also shows the formation of nanocrystalline grains, due to static grain refinement by severe plastic deformation, close to the running rail surface. The variation of crystal orientation along the direction of depth, in the common fibre textures, was plotted in Fig. 10. It can be seen that the strong {110} texture was developed close to the running surface, up to ≈ 80 μm, at the transition region between nanocrystalline WEL and non-deformed rail structure. Wang et al. [60] reported that grains containing a high quantity of sub-grain boundaries were usually oriented along, or close to, the <110> axis of crystal orientations. The reason lies in the fact that lattice dislocation (i.e., nucleation, multiplication, and motion of dislocations), responsible for plastic deformation, glide on compact crystal planes and directions within the lattice. Thus, dislocation pile-ups, dynamic recovery and formation of sub-grains subsequently occur in {110} oriented grains. The other grain orientations were identified at increased distances from the running surface. The {111} and {100} grain orientations found, are common in hot-rolled processing, during rail fabrication and post-treatment, and are in agreement with the previous results of macro-texture analysis.

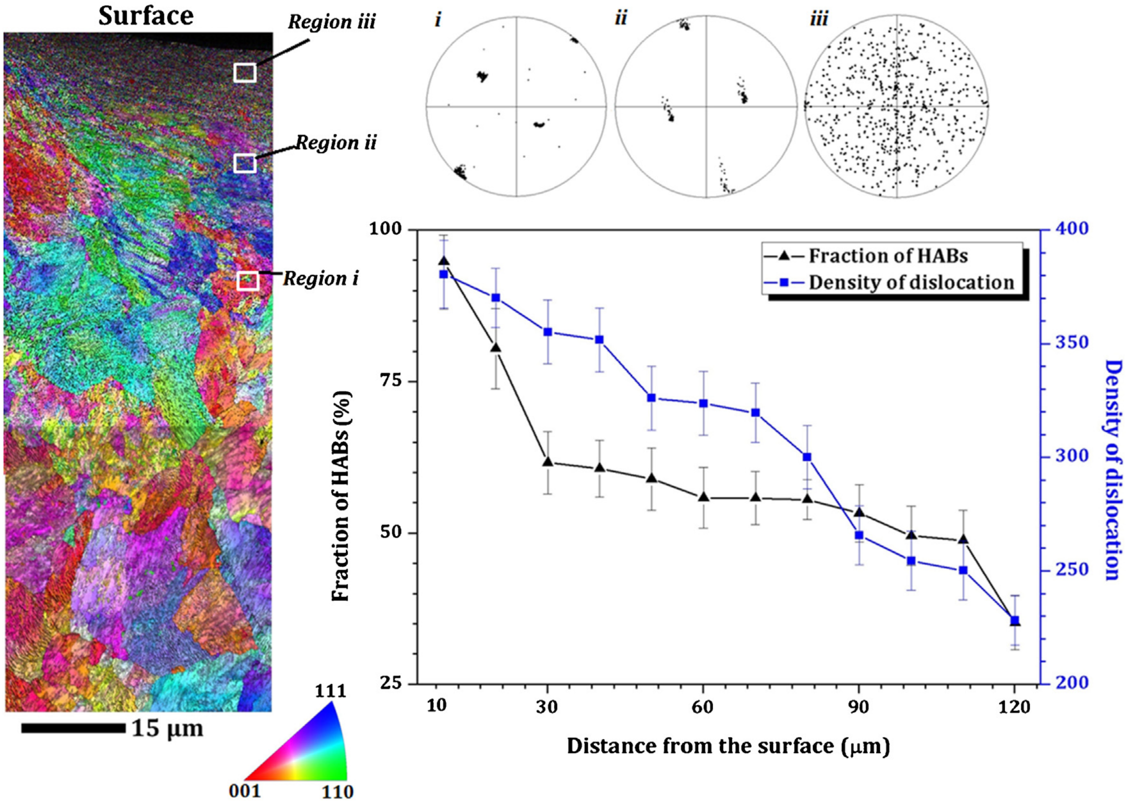

Fig. 9 – Variation of crystal orientation, fraction of HABs and dislocation density changes along normal direction of used rail sample.

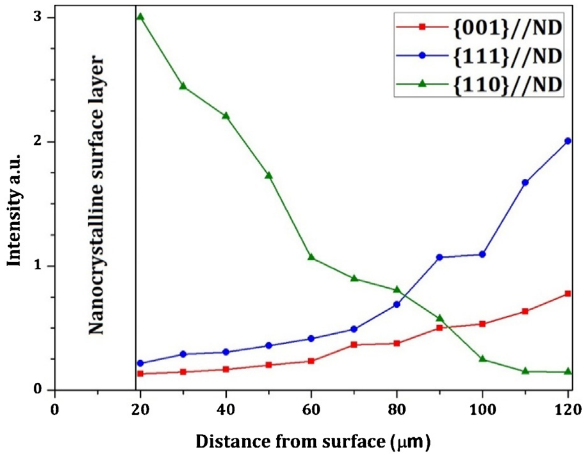

Fig. 10 – Variation of grain orientations as a function of distance from the surface referred to Fig. 9.

The experimental results from the reduced Young's modulus and nano-hardness with internal energy and formation of ultrafine grains, obtained from EBSD data, can be explained by the good behaviour of rail steel under intense cyclic stress-strain in the railway operations after approximately 30 MTBT. However, cementite dissolution, during severe plastic deformation, forms the superficial, featureless white layer structure up to approximately 20 μm depth from the contact rail surface. Moreover, nano-hardness testing demonstrated that the development of compressive residual stress on the rail surface, due to rolling/sliding loading, could enhance micro-crack nucleation. Sato et al. [61] reported that superficial fatigue cracks initiated and extended in the region with minimum tensile stress (i.e., earlier plastic flow) along railroad lines, rather than in the normal regions. Moreover, plastic flow stress in metals, depends on the transferability of dislocations through grain boundaries, which also considers both the crystallographic orientation of slip systems and the applied stress. The set of macrotexture and EBSD data indicates the predominance of {110} crystallographic texture from the subsurface to about ≈80 μm depth from the surface. Kamaya et al. [62] reported that the crystal orientation is a dominant factor which can influence Young's modulus in polycrystalline materials. Sainath et al. [54] showed that if Young's modulus is highest in the {110} direction, this helps to achieve the greatest ductility (i.e., combination of the highest ultimate, yield strength, and elongation) in BCC materials.

4. Conclusions

The evolution of microstructure and crystallographic orientations as a function of distance depth of a used rail sample, removed from a heavy-haul Brazilian railroad, was studied by various techniques. Characterisation of a very thin nanocrystalline carbon supersaturated α-iron phase at the contact rail, and the variation of microstructural features along the depth distance, were the main aims of this paper to help determine good wear resistance of the used rail after 30 MTBT. The following conclusions can be drawn:

- Diverse pearlite microstructures containing featureless, fragmented, aligned, thinning and bending, were characterised along the depth distance of the rail surface as a result of shear and normal stress.
- Microhardness and nano-indentation hardness values reached approximately 835 ± 15 HV and 7.9 GPa very close to the rail surface (≈10 μm distance depth).
- Characterisation of the presence of a carbon supersaturated α-iron phase, at the very thin (≈15 μm) WEL region, showed it to contain about 3.78 %C saturated in the ferrite phase.
- Presence of a dominant {110} crystallographic texture, with a high Young's modulus, close to the rail surface at the transition region between nanocrystalline WEL and non-deformed rail structure, could retard crack formation and increase wear resistance.

Conflict of interest and authorship conformation form

Please check the following as appropriate:

- All authors have participated in (a) conception and design, or analysis and interpretation of the data; (b) drafting the article or revising it critically for important intellectual content; and (c) approval of the final version.
- This manuscript has not been submitted to, nor is under review at, another journal or other publishing venue.
- The authors have no affiliation with any organization with a direct or indirect financial interest in the subject matter discussed in the manuscript
- The following authors have affiliations with organizations with direct or indirect financial interest in the subject matter discussed in the manuscript:

Acknowledgements

The authors would like to thank Vale Institute of Technology (ITV) and Wheel-Rail Chair for the financial support.

REFERENCES

[1] Clayton P, Danks D. Effect of interlamellar spacing on the wear resistance of eutectoid steels under rolling-sliding conditions. Wear 1990;135:369–89.

[2] Chandrasekaran KA, Natarajan T, Kishore T. Influence of microstructure on the wear of grinding media. Wear 1991;147:267–74.

[3] Das Bakshi S. Wear of fine pearlite, nanostructured bainite and martensite, University of Cambridge; 2016.

[4] Katsuki F, Yonemura M. Subsurface characteristics of an abraded Fe-0.4wt%C pearlitic steel: a nanoindentation study. Wear 2007;263:1575–8, http://dx.doi.org/10.1016/j.wear.2007.01.092.

[5] Olivares RO, Garcia CI, DeArdo A, Kalay S, Robles Hernández FC. Advanced metallurgical alloy design and thermomechanical processing for rails steels for North American heavy haul use. Wear 2011;271:364–73, http://dx.doi.org/10.1016/j.wear.2010.10.048.

[6] Korbel A, Bochniak W. Stratified plastic flow in metals. Int. J. Mech. Sci 2017;129:269–76, http://dx.doi.org/10.1016/j.ijmecsci.2017.04.006.

[7] Olivares RO. Study of the austenite decomposition and formation of proeutectoid cementite in hyper-eutectoid steels; 2011. p. 143.

[8] Österle W, Rooch H, Pyzalla A, Wang L. Investigation of white etching layers on rails by optical microscopy, electron microscopy, X-ray and synchrotron X-ray diffraction. Mater Sci Eng A 2001;303:150–7, http://dx.doi.org/10.1016/S0921-5093(00)01842-6.

[9] Milman YV, Grinkevych KE, Chugunova SI, Lojkowski W, Djahanbakhsh M, Fecht HJ. Tribological properties of the surface of railway tracks, studied by indentation technique. Wear 2005;258:77–82, http://dx.doi.org/10.1016/j.wear.2004.02.017.

[10] Takahashi J, Kawakami K, Ueda M. Atom probe tomography analysis of the white etching layer in a rail track surface. Acta Mater 2010;58:3602–12, http://dx.doi.org/10.1016/j.actamat.2010.02.030.

[11] Wu J, Petrov RH, Naeimi M, Li Z, Dollevoet R, Sietsma J. Laboratory simulation of martensite formation of white etching layer in rail steel. Int J Fatigue 2016;91:11–20, http://dx.doi.org/10.1016/j.ijfatigue.2016.05.016.

[12] Lojkowski W, Djahanbakhsh M, Burkle G, Gierlotka S, Zielinski W, Fecht HJ. Nanostructure formation on the surface of railroad tracks. Mater Sci Eng A 2001;303:197–208.

[13] Chen H, Zhang C, Liu W, Li Q, Zhigang Y. Microstructural evolution of a hypoeutectoid pearlite steel under rolling-sliding contact loading. J Iron Steel Res Int 2016;23:1054–60, http://dx.doi.org/10.1016/S1006-706X(16)30157-1.

[14] Sauvage X, Lefebvre W, Genevois C, Ohsaki S, Hono K. Complementary use of transmission electron microscopy and atom probe tomography for the investigation of steels nanostructured by severe plastic deformation. Scr Mater 2009;60:1056–61, http://dx.doi.org/10.1016/j.scriptamat.2009.02.019.

[15] Borchers C, Kirchheim R. Cold-drawn pearlitic steel wires. Prog Mater Sci 2016;82:405–44, http://dx.doi.org/10.1016/j.pmatsci.2016.06.001.

[16] Olofsson U, Telliskivi T. Wear, plastic deformation and friction of two rail steels—a full-scale test and a laboratory study. Wear 2003;254:80–93.

[17] Olofsson U, Andersson S, Bjorklund S. Simulation of mild wear in boundary lubricated spherical roller thrust bearings. Wear 2000;241:180–5.

[18] De Bellefon GM, Van Duysen JC. Tailoring plasticity of austenitic stainless steels for nuclear applications: review of mechanisms controlling plasticity of austenitic steels below 400 C. J Nucl Phys Mater Sci Radiat Appl 2016;475:168–91, http://dx.doi.org/10.1016/j.jnucmat.2016.04.015.

[19] Po G, Cui Y, Rivera D, Cereceda D, Swinburne TD, Marian J, et al. A phenomenological dislocation mobility law for bcc metals. Acta Mater 2016;119:123–35.

[20] Chen P, Mao SC, Liu Y, Wang F, Zhang YF, Zhang Z, et al. In-situ EBSD study of the active slip systems and lattice rotation behavior of surface grains in aluminum alloy during tensile deformation. Mater Sci Eng A 2013;580:114–24.

[21] Calcagnotto M, Ponge D, Demir E, Raabe D. Orientation gradients and geometrically necessary dislocations in ultrafine grained dual-phase steels studied by 2D and 3D EBSD. Mater Sci Eng A 2010;527:2738–46, http://dx.doi.org/10.1016/j.msea.2010.01.004.

[22] Satoh Y, Iwafuchi K. Crystal orientation analysis of running surface of rail damaged by rolling contact. Wear

2005;258:1126–34, http://dx.doi.org/10.1016/j.wear.2004.03.048.

[23] Dylewski B, Risbet M, Bouvier S. The tridimensional gradient of microstructure in worn rails – experimental characterization of plastic deformation accumulated by RCF. Wear 2017;392–393:50–9, http://dx.doi.org/10.1016/j.wear.2017.09.001.

[24] Matsuda H, Satoh Y, Kanematsu Y, Iwafuchi K. On-site investigation and analysis of flaking damage leading to rail break. Wear 2011;271:168–73, http://dx.doi.org/10.1016/j.wear.2010.10.041.

[25] Guo N, Song B, Luan B, Chen Z, Liu Q. Deformation bands in fully pearlitic steel during wire drawing. Sci China Ser A-mathematics Phys Astron Technol Sci 2014;57:796–803, http://dx.doi.org/10.1007/s11431-013-5434-8.

[26] Solano-Alvarez W. Microstructural degradation of bearing steels. University of Cambridge; 2014.

[27] Wetscher F, Stock R, Pippan R. Changes in the mechanical properties of a pearlitic steel due to large shear deformation. Mater Sci Eng A 2007;445–446:237–43, http://dx.doi.org/10.1016/j.msea.2006.09.026.

[28] Dao M, Chollacoop N, Vliet KJV, Venkatesh TA, Suresh S. Computational modeling of the forward and reverse problems in instrumented sharp identatiob. Acta Mater 2001;49:3899–918, http://dx.doi.org/10.1016/S1359-6454(01)00295-6.

[29] Caglioti G, Paoletti A, Ricci FP. Choice of collimators for a crystal spectrometer for neutron diffraction. Nucl Instruments 1958;3:223–8.

[30] Das Bakshi S, Leiro A, Prakash B, Bhadeshia HKDH. Dry rolling/sliding wear of nanostructured pearlite. Mater Sci Technol 2015;31:1735–44, http://dx.doi.org/10.1179/1743284714Y.0000000751.

[31] Lee S, Lee Y. Quantitative analyses of ferrite lattice parameter and solute Nb content in low carbon microalloyed steels. Scr Mater 2005;52:973–6, http://dx.doi.org/10.1016/j.scriptamat.2005.01.028.

[32] Bachmann F, Hielscher R, Schaeben H. Ultramicroscopy Grain detection from 2d and 3d EBSD data — specification of the MTEX algorithm. Ultramicroscopy 2011;111:1720–33, http://dx.doi.org/10.1016/j.ultramic.2011.08.002.

[33] Godefroid LB, Moreira LP, Vilela TCG, Faria GL, Candido LC, Pinto ES. Effect of chemical composition and microstructure on the fatigue crack growth resistance of pearlitic steels for railroad application. Int J Fatigue 2019;120:241–53, http://dx.doi.org/10.1016/j.ijfatigue.2018.10.016.

[34] Nakada N, Koga N, Tanaka Y, Takaki S, Ueda M. Strengthening of pearlitic steel by Ferrite/Cementite elastic misfit strain. ISIJ Int 2015;55:2036–8.

[35] Gladman T, Mclvor I, Pickering F. Some aspects of the structure-property relationshps in high-carbon ferrite-pearlite steels. J Iron Steel Res Int 2017;210(2017).

[36] Toribio J, Matos JC, Ayaso FJ. Role of the microstructure on the mechanical properties of fully pearlitic eutectoid steels. Frat Ed Integrità Strutt 2014;30:424–30, http://dx.doi.org/10.3221/IGF-ESIS.30.51.

[37] Hall EO. The deformation and ageing of mild steel. Proc Phys Soc London Sect B 1951;64:747–53, http://dx.doi.org/10.1088/0370-1301/64/9/303.

[38] Wen Z, Wu L, Li W, Jin X, Zhu M. Three-dimensional elastic-plastic stress analysis of wheel-rail rolling contact. Wear 2011;271:426–36, http://dx.doi.org/10.1016/j.wear.2010.10.001.

[39] Reuben RL. Monitoring of rail-wheel interaction using acoustic emission (AE). Adv Mater Res 2006;13:1–24, http://dx.doi.org/10.4028/www.scientific.net/AMR.13-14.161.

[40] Toribio J. Relationship between microstructure and strength in eutectoid steels. Mater Sci Eng A 2004;389:227–30, http://dx.doi.org/10.1016/j.msea.2004.01.084.

[41] Ning G, Baifeng L, Bingshu W, Qing L. Microstructure and texture evolution in fully pearlitic steel during wire drawing. Sci China Ser A-mathematics Phys Astron Technol Sci 2013;56:1139–46, http://dx.doi.org/10.1007/s11431-013-5184-7.

[42] Embury JD, Fisher RM. The structure and properties of drawn pearlite. Acta Metall 1966;14:147–59, http://dx.doi.org/10.1016/0001-6160(66)90296-3.

[43] Warhadpande A, Sadeghi F, Evans RD. Microstructural alterations in bearing steels under rolling contact fatigue. Tribol Trans 2014;57:66–76.

[44] Fischer-Cripps AC. Nanoindentation. Springer-Verlag New York; 2011, http://dx.doi.org/10.1007/978-1-4419-9872-9.

[45] Chen Z, Colliander MH, Sundell G, Peng RL, Zhou J, Johansson S, et al. Nano-scale characterization of white layer in broached Inconel 718. Mater Sci Eng A 2017;684:373–84, http://dx.doi.org/10.1016/j.msea.2016.12.045.

[46] Masumoto H, Kikuchi M. Elastic Anisotropy and Its Temperature Dependence of the Single Crystals of Fe-19.43 % Cr Alloy. Trans Japan Inst Met 1971;12:90–5.

[47] Seo J, Kwon S, Jun H, Lee D. Numerical stress analysis and rolling contact fatigue of White Etching Layer on rail steel. Int J Fatigue 2011;33:203–11, http://dx.doi.org/10.1016/j.ijfatigue.2010.08.007.

[48] Wang Y, Yuan L, Zhang S, Sun C, Wang W. The influence of combined gradient structure with residual stress on crack-growth behavior in medium carbon steel. Eng Fract Mech 2019;209:369–81.

[49] Garcia-mateo C. Carbon concentration measurements by atom probe tomography in the ferritic phase of high- silicon steels. Acta Mater 2016;125:359–68, http://dx.doi.org/10.1016/j.actamat.2016.12.013.

[50] Nematollahi GA, Pezold JV, Raabe D. Thermodynamics of carbon solubility in ferrite and vacancy formation in cementite in strained pearlite. Acta Mater 2013;61:1773–84.

[51] Li YJ, Choi P, Borchers C, Westerkamp S, Goto S, Raabe D, et al. Atomic-scale mechanisms of deformation- induced cementite decomposition in pearlite. Acta Mater 2011;59:3965–77, http://dx.doi.org/10.1016/j.actamat.2011.03.022.

[52] Guo N, Song B, Wang BS, Liu Q. Influence of torsion deformation on textures of cold drawing pearlitic steel wires. Acta Metall Sin (English Lett 2015;28:707–14, http://dx.doi.org/10.1007/s40195-015-0251-7.

[53] Suwas S, Ray RK. Deformation textures. In: Crystallogr. Texture Mater., engineerin. Springer US; 2014. p. 95–141.

[54] Sainath G, Choudhary BK. Orientation dependent deformation behaviour of BCC iron nanowires. Comput Mater Sci 2016;111:406–15, http://dx.doi.org/10.1016/j.commatsci.2015.09.055.

[55] Blondé R, Jimenez-Melero E, Zhao L, Wright JP, Brück E, Van Der Zwaag S, et al. High-energy X-ray diffraction study on the temperature-dependent mechanical stability of retained austenite in low-alloyed TRIP steels. Acta Mater 2012;60:565–77, http://dx.doi.org/10.1016/j.actamat.2011.10.019.

[56] Ruggles TJ, Fullwood DT. Estimations of bulk geometrically necessary dislocation density using high resolution EBSD. Ultramicroscopy 2013;133:8–15, http://dx.doi.org/10.1016/j.ultramic.2013.04.011.

[57] Bracquart B, Mareau C, Saintier N, Morel F. Experimental study of the impact of geometrical defects on the high cycle fatigue behavior of polycrystalline aluminium with di ff erent grain sizes. Int J Fatigue 2018;109:17–25, http://dx.doi.org/10.1016/j.ijfatigue.2017.12.009.

[58] Wan VVC, Jiang J, Maclachlan DW, Dunne FPE. Microstructure-sensitive fatigue crack nucleation in a polycrystalline Ni superalloy. Int J Fatigue 2016;90:181–90.

[59] Masoumi M, Ariza EA, Sinatora A, Goldenstein H. Role of crystallographic orientation and grain boundaries in fatigue

crack propagation in used pearlitic rail steel. Mater Sci Eng A 2018;722:147–55, http://dx.doi.org/10.1016/j.msea.2018.03.028.

[60] Wang Y, Ringer S, Zhu YT. Mechanism of grain growth during severe plastic deformation of a nanocrystalline Ni – Fe alloy. Appl Phys Lett 2009;94:11908–12, http://dx.doi.org/10.1063/1.3065025.

[61] Sato M, Anderson PM, Rigney DA. Rolling-sliding behavior of rail steels. Wear 1993;164:159–72.

[62] Kamaya M. A procedure for estimating Young's modulus of textured polycrystalline materials. Int J Solids Struct 2009;46:2642–9, http://dx.doi.org/10.1016/j.ijsolstr.2009.02.013.